Advanced Functional Materials

ADVANCED FUNCTIONAL MATERIALS
www.afm-journal.de

RESEARCH ARTICLE OPEN ACCESS

Statistically Resolving Thickness-Dependent Electrical Characteristics in Multilayer-MoS_2 Transistors

Sanghyun Lee[1] | Sumin Hong[1] | Minho Park[2] | Seongju Kim[3] | Sanghoon Baek[4] | Seonguk Yang[5] | Chang-Soo Lee[6] | Sang-Hoon Bae[7] | Joonki Suh[5] | Yongwoo Lee[2,8] | Haksoon Jung[2,8] | Jimin Kwon[1,2,8]

[1]Graduate School of Semiconductor Materials and Devices Engineering, Ulsan National Institute of Science and Technology (UNIST), Ulsan, Republic of Korea | [2]Department of Electrical Engineering, Ulsan National Institute of Science and Technology (UNIST), Ulsan, Republic of Korea | [3]Department of Creative Convergence Engineering, Hanbat National University, Daejeon, Republic of Korea | [4]Department of Biomedical Engineering, Hanyang University, Seoul, Republic of Korea | [5]Department of Chemical and Biomolecular Engineering, Korea Advanced Institute of Science and Technology (KAIST), Daejeon, Republic of Korea | [6]TDS Innovation, Daejeon, Republic of Korea | [7]Department of Mechanical Engineering and Materials Science, Washington University in St. Louis, St. Louis, Missouri, USA | [8]School of Electrical Engineering, Korea Advanced Institute of Science and Technology (KAIST), Daejeon, Republic of Korea

Correspondence: Yongwoo Lee (ywlee96@kaist.ac.kr) | Haksoon Jung (hsjung71@kaist.ac.kr) | Jimin Kwon (jmkwon@kaist.ac.kr)

Received: 31 December 2025 | **Revised:** 10 March 2026 | **Accepted:** 11 March 2026

Keywords: automatic flake detection | optical classification | single-flake transistors | transition metal dichalcogenides (TMDs)

ABSTRACT

Atomically thin 2D semiconductors enable excellent electrostatic control even in highly scaled transistors with few-nanometer gate lengths. The electrical characteristics of 2D transistors can vary significantly with the number of layers, yet how device behavior evolves with channel thickness remains statistically unexplored. This limitation mainly arises from the difficulty of obtaining large numbers of single-crystal flakes with well-controlled thickness and fabricating devices. Here, we demonstrate the thickness-dependent electrical characteristics of single-flake MoS_2 transistors correlating optical observables with the monolayer (ML) numbers. The optical intensity serves as an indicator of flake thickness for identifying the number of MLs, while algorithm-based filtering of blurry edges and non-uniform intensities enables the selection of high-quality flakes. The filtered flakes are subsequently grouped into distinct thickness clusters based on their optical intensity distributions. The resulting thickness clusters are validated by atomic force microscopy, yielding flakes spanning 3–8 MLs. Automated device layout generation allows the electrical characterization of 1615 transistors selected from over 120000 flakes, providing insight into thickness-dependent charge carrier injection and transport behavior. Our findings offer a statistically grounded framework linking flake thickness to electrical characteristics and demonstrate the utility of readily accessible optical microscopy for accelerating 2D semiconductor device research.

1 | Introduction

Two-dimensional (2D) transition metal dichalcogenides (TMDs), with atomically thin bodies and superior electrostatic control, represent a fundamental shift in electronic materials beyond the scaling limits of silicon technology [1–4]. Unlike bulk semiconductors, the dangling bond-free surfaces of 2D semiconductor materials offer exceptional electrical characteristics, as surface state-induced field-effect mobility degradation is suppressed even at sub-nanometer thicknesses [5]. The scaling-suitable atomic structures, facilitated by van-der Waals gaps, introduce them as promising candidates for next-generation logic, and memory channel materials [6–9].

Among 2D TMD materials, MoS_2 stands out as a promising channel material owing to its sizable bandgap E_g, and excellent

electrical properties. A 0.65-nm-thick monolayer (ML) MoS_2 possesses an E_g of 1.9 eV [5, 10], and exhibits a high field-effect mobility of 200 $cm^2/V{\cdot}s$ and a large on-off ratio exceeding 10^8 [11]. As in other nanoscale semiconductor systems such as quantum dots and nanotubes, the E_g of atomically thin MoS_2 can vary significantly due to quantum confinement effects [12–14], decreasing to approximately 1.2 eV as MoS_2 transitions to its bulk form. This thickness-dependent band structure modulation provides a powerful means to tune electronic and transport properties in 2D semiconductor devices. In addition to bandgap variation, increasing the number of layers also modifies carrier screening, interlayer coupling, and electrostatic gate controllability within the channel. These effects directly influence key transistor parameters such as threshold voltage, contact resistance, subthreshold swing, and current drive capability.

Although theoretical [15–17] and optical studies [18–20] have explored thickness-dependent properties of 2D materials, empirical investigations of thickness-dependent device characteristics are still scarce. Systematic experimental studies are challenging because mechanically or electrochemically exfoliated flakes are typically distributed randomly across the substrate and exhibit significant thickness variations [21, 22]. As a result, the channel thickness of most fabricated devices is determined in a largely uncontrolled manner, making direct comparison of device characteristics across different layer numbers difficult. Even when 2D materials are synthesized through chemical vapor deposition (CVD), systematic investigation of thickness-dependent device characteristics remains challenging. CVD growth typically produces monolayer or few-layer domains with relatively uniform thickness across the substrate, making it difficult to obtain devices spanning a wide range of layer numbers from a single growth process [23, 24].

Recent studies have attempted to detect and characterize individual flakes using image-processing approaches [25–31]. However, acquiring statistically meaningful large datasets and performing device-level electrical characterization across multiple thicknesses remains challenging. In particular, the identification of suitable flakes, the determination of their thickness, and the subsequent device layout design often rely heavily on manual inspection, which severely limits throughput and scalability. Therefore, scalable approaches that can automatically identify flakes, classify their thickness, and integrate them into device fabrication workflows are essential for establishing statistically robust relationships between layer thickness and electronic transport behavior in 2D materials.

In this work, we present an integrated framework for optical flake identification and large-scale transistor fabrication based on electrochemically exfoliated MoS_2 single flakes. By separating red (R), green (G), and blue (B) channels from optical microscopy images, a clustering parameter associated with the ML number is introduced, and the thickness assignment is validated through direct correlation with atomic force microscopy (AFM) measurements. Using the optically extracted flake coordinate data, custom electrode layouts are automatically generated to enable large-scale device fabrication. We fabricate and electrically characterize 1615 field-effect transistors (FETs) selected from over 120 000 classified flakes, providing statistically resolved access to thickness-dependent transport behavior. This study establishes an empirical relationship between layer thickness and charge transport in MoS_2 transistors and provides a statistically robust dataset for understanding thickness-dependent device physics in 2D semiconductors, offering a scalable foundation for both nanometric device research and large-scale integration.

2 | Results and Discussion

Exfoliated MoS_2 flakes were characterized by a random thickness distribution and an irregular spatial arrangement over a 1.5 × 1.5 cm substrate (Figure 1a). In total, 74 119 flakes were identified, each represented as a point corresponding to its thickness level classification from 1 to 6. The specific coating method is detailed in the Experimental section. Despite their nanometer-scale thickness, the flakes exhibit high optical visibility, enabling identification through conventional optical microscopy. MoS_2 flakes, obtained via an electrochemical intercalation-based exfoliation (Figure S1), were optically inspected and grouped into 6 levels based on their RGB intensity contrast (Figure 1b). Upon decomposition into individual color channels, the RGB histograms exhibit distinct intensities, particularly within the RG channels. The average optical intensity contrast values in each flake for Levels 1 through 6 were obtained as 0.0299, 0.0446, 0.0644, 0.0765, 0.0813, and 0.0960 for the white channel, and 0.0195, 0.0337, 0.0444, 0.0772, 0.0873, and 0.1206 for the R channel, respectively. Similarly, the G channel yielded contrast values of 0.0365, 0.0679, 0.1070, 0.1383, 0.1571, and 0.1939, while the B channel displayed values of 0.0371, 0.0457, 0.0656, 0.0575, 0.0391, and −0.0083. The negative value in the B channel at Level 6 is attributed to the normalization process relative to the substrate.

The optical pixel intensity correlates with flake thickness, as the contrast between the substrate and the flakes increases discretely, corresponding to the quantized thickness characteristic of layered 2D materials. Through the screening process, 403 high-quality flakes were isolated based on the absence of observable residues, wrinkles, or folds (Figure 1c). Automated flake localization, alignment, and routing procedures were then used to generate source/drain electrodes and routing masks that are deterministically aligned to each identified flake (Figure 1d; Figure S2 and Note S1). Specific clustering protocols and thickness validation will be addressed in Figure 3 in detail. This approach enables the fabrication of large numbers of nominally identical transistors at each thickness. The electrical characteristics were subsequently analyzed and systematically correlated with the optically inferred layer number (Figure 1e). Lastly, the large-scale screening and subsequent device integration have been achieved, providing a robust platform for the acquisition of extensive statistical data.

An image-processing workflow was developed to identify flakes and automatically generate device layouts across the substrate, enabling large-scale device fabrication from optical image datasets (Figure 2a). Alignment marks were patterned on the bare substrate to provide an accurate reference position during image analysis. Thick metal patterns were introduced only at the electrode pad regions to ensure robust electrical contact, while thinner metal near the channel preserved fine pattern definition.

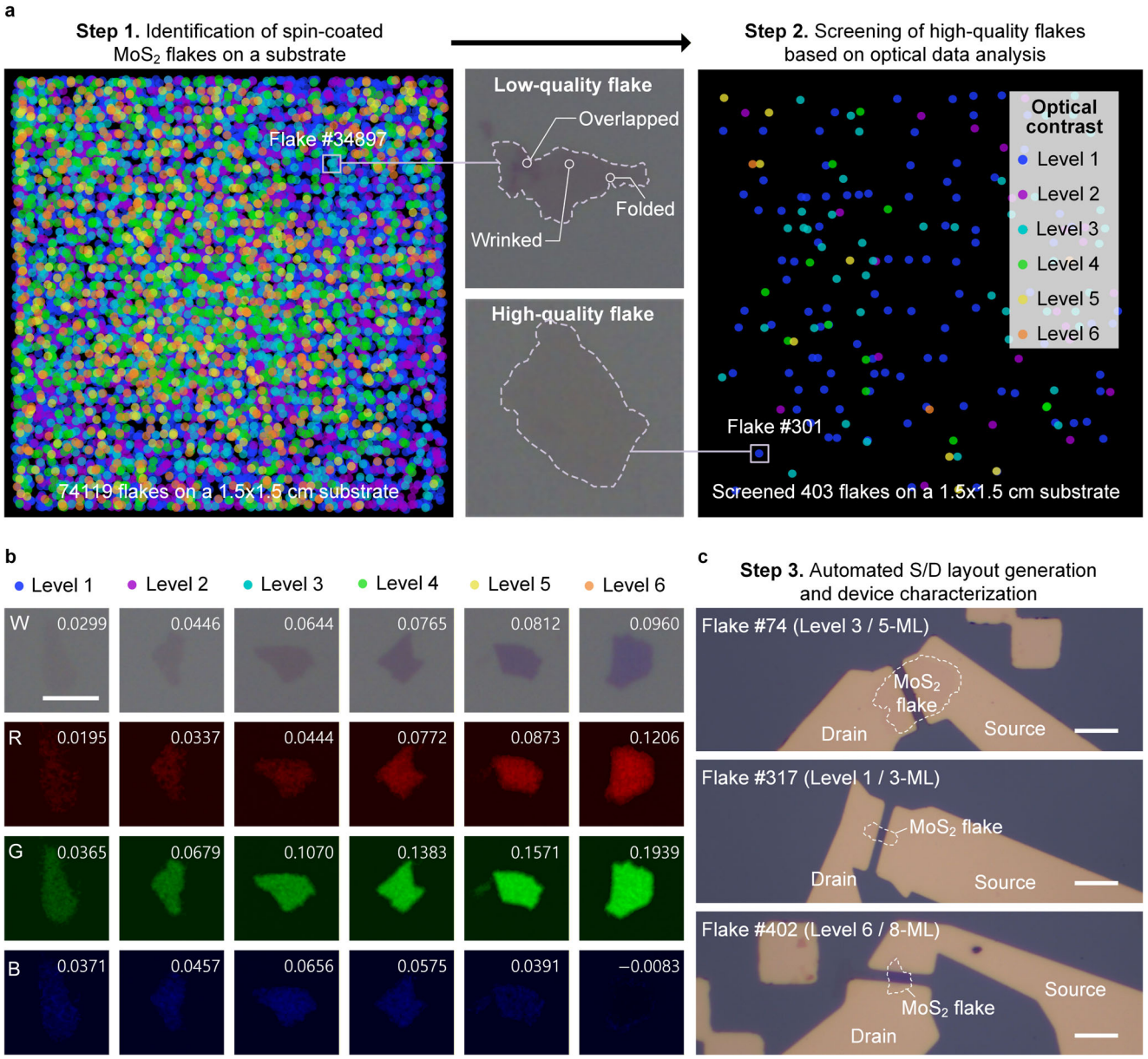

FIGURE 1 | Optical MoS_2 flake identification and thickness-dependent characterization. (a) 74,119 spin-coated MoS_2 flakes mapped across a 1.5 × 1.5 cm substrate were screened to obtain high-quality 403 flakes based on optical intensities in R, G, and B channel images. The flakes were classified from Level 1 to 6 based on optical intensities in the R, G, and B channel images. Blue, purple, cyan, green, yellow, and orange solid circles correspond to Level 1, 2, 3, 4, 5, and 6, respectively. Low-quality flake exhibited wrinkled, folded, or overlapped features, while high-quality flake displayed a neat surface suitable for device fabrication (scale bar is 5 μm). (b) white, R, G, and B channel images representing mean optical intensity values of flakes (scale bar is 5 μm). (c) OM images of MoS_2 single-flake transistors using flake #74 (Level 3/5-ML MoS_2), #317 (Level 1/3-ML MoS_2), and #402 (Level 6/8-ML MoS_2). L_{ch} was fixed to 3 μm, and the W_{ch} of flakes was normalized in *I-V* characteristics.

First, the acquired color images were converted to grayscale to enhance edge detection efficiency, followed by illumination correction to flatten non-planar brightness variations across each image (Figure 2b). The non-uniform intensity was primarily caused by vignetting, where brightness decreases toward the image edges due to the microscope's lens characteristics. Accordingly, flake boundaries were extracted by intensity binarization, using a threshold determined from the background to define sharp profiles. In this step, noise arising from small-area detections (<500 pixels) and low-solidity regions, which are likely to originate from small particle contamination or irregular intensity fluctuations, was ignored to refine the flake identification processes. The flake parameters such as representative RGB intensity values, orientation angles, lateral dimensions, surface quality, and absolute global coordinates were extracted (Figure S3). The high-quality flakes were selected based on their ability to accommodate specific device geometries, where the contact length and gate length correspond to the electrode width and spacing, respectively, and the channel width was determined by the resulting electrode structure and the maximum available length of the flake. A tilt correction provides accurate global localization of each flake across the substrate using the global coordinates obtained in the preceding step. Based on the coordinates, the source/drain patterns were algorithmically positioned for each

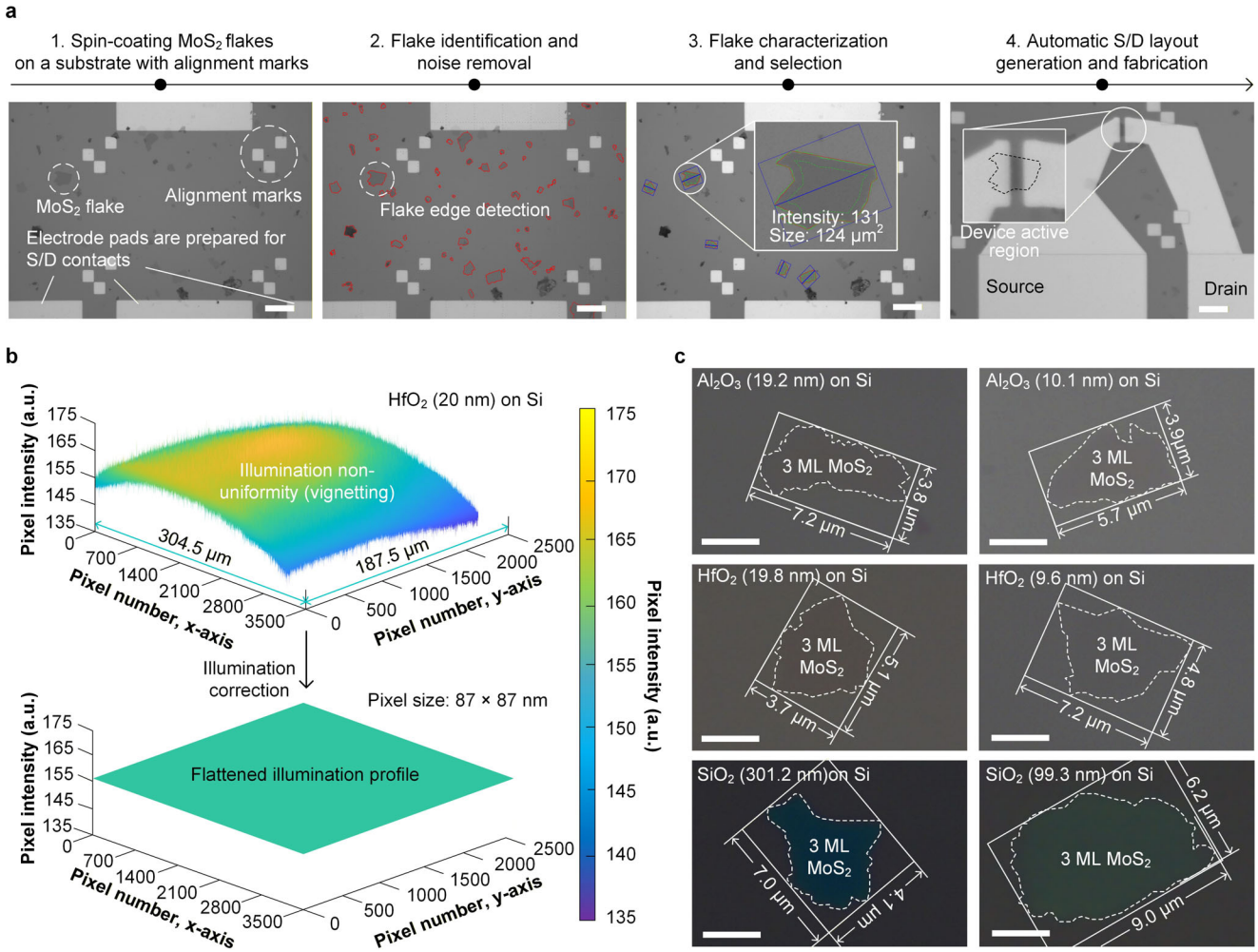

FIGURE 2 | Automated image preprocessing and device layout generation for consistent and substrate-universal flake characterization. (a) Single-image preprocessing for flake edge detection, optical characterization, and automated source-drain device layout generation (scale bar is 25 μm). (b) Brightness gradient correction within the image is caused by variations in the microscope illumination distance. (c) 3-ML MoS_2 flakes on Al_2O_3, HfO_2, and SiO_2 dielectrics (scale bar is 2 μm).

flake. The electrode geometry was rotated to match the angle of the flake, and routing paths are automatically generated to connect the source/drain electrodes to the corresponding contact electrode pads.

The flake identification was achieved across different substrate materials and thicknesses. The representative optical images of 3-ML MoS_2 flakes on different substrates are shown in Figure 2c, including ALD-grown Al_2O_3 (19.2 and 10.1 nm), ALD-grown HfO_2 (19.8 and 9.6 nm), and thermally grown SiO_2 (301.2 and 99.3 nm). The optical responses varied with the energy bandgap and the substrate thickness, resulting in differences in color, and RGB values. Flake detection relied on the grayscale contrast between the flake and the substrate to mitigate variations in RGB values. The optical and geometrical parameters of individual flakes were extracted to enable substrate-independent flake localization across different substrate materials and thicknesses (Figure S3 and Tables S1–S3). Notably, the same automated detection, characterization, and routing workflow was applied not only to solution-processed, electrochemically exfoliated MoS_2 flakes but also to MoS_2 flakes grown by metal–organic chemical vapor deposition (Figure S4).

The optical intensity analysis was performed within a predefined inner region of each flake to avoid edge-related artifacts (Figure 3a). To construct reliable pixel-intensity histograms, a boundary margin corresponding to 20% of the total flake area was removed, retaining the inner 80% as the valid region. High-quality flakes exhibited a single narrow intensity peak fitted by a Gaussian distribution peak function, whereas contaminated or locally folded flakes produced broader distributions and multiple peaks (Table S4). A screening factor, $S = I_{P,max} - I_{P,min}$, was introduced to quantify the grayscale intensity variation within each flake.

Layer-dependent intensity clusters were clearly distinguished in the RG-channel intensity space of MoS_2 flakes (Figure 3b). The RG-channel intensity mapping of 74 119 MoS_2 flakes on a 20 nm HfO_2 substrate revealed multiple separated intensity peaks corresponding to different layer numbers under varying S conditions. In contrast, the B channel showed negligible layer-dependent clustering compared to the R and G channels (Figure S5). A hybrid clustering approach combining density-based spatial clustering of applications with noise (DBSCAN) and a Gaussian mixture model (GMM) analysis was employed to classify these layer-dependent intensity groups. DBSCAN was

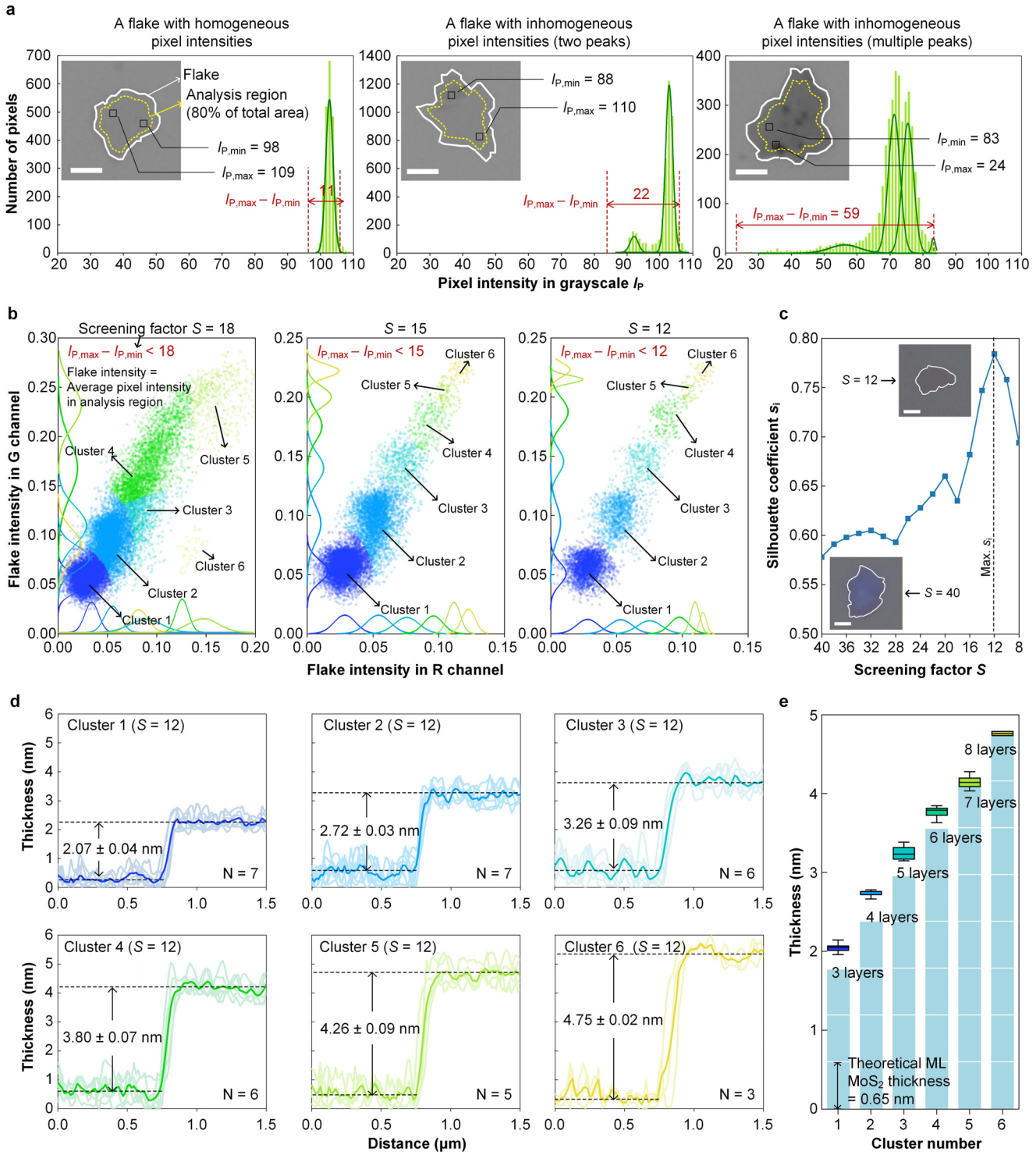

FIGURE 3 | Flake screening factor S and RG-channel intensity clusters correspond to MoS_2 layer numbers. (a) Flake S is determined by internal intensity variation and peak count. Inset shows the optical image of the representative flakes exhibiting high, medium, and low S. Scale bar is 4 μm. (b) RG-channel intensity distributions of 74 119 flakes categorized by screening-factor levels, including marginal inner-cluster distribution profiles along the R and G-channel intensity axes. (c) Silhouette-coefficient dependence on the S. Inset shows the optical image of the flake corresponding to S of 40 (left) and 12 (right) (scale bar is 4 μm). (d) AFM measured height profile of MoS_2 flake for each cluster. N is the number of measured devices. (e) MoS_2 layer numbers corresponding to the AFM measured flake thicknesses for each cluster.

first applied to remove locally isolated points in intensity space as noise. The remaining data were then analyzed using a GMM with full covariance matrices to capture the correlated distribution of R and G-channel intensities. The GMM models the overall probability density function $p(x)$ as a weighted sum of multiple Gaussian components, expressed as

$$p(x) = \sum_{k=1}^{K} \pi_k N(x|\mu_k, \Sigma_k)$$

where μ_k and Σ_k denote the mean vector and covariance matrix of the k_{th} cluster, respectively. At $S = 18$, the cluster boundaries were ambiguous, and adjacent clusters partially overlapped. Independent analysis of the probability density distributions along the R and G axes revealed substantial inter-cluster overlaps in both channels, indicating limited separation between cluster centroids. As the S decreased below 15, the cluster boundaries became progressively clearer, and the marginal distributions narrowed. The most pronounced cluster separation was obtained at $S = 12$, where distinct RG-channel intensity groups emerged. Clustering quality was evaluated using the silhouette coefficient s_i, reflecting cluster cohesion and separation. For a given data point i, s_i is defined as

$$s_i = \frac{b_i - a_i}{\max(a_i, b_i)}$$

where a_i represents the average distance between point i and other points within the same cluster, and b_i denotes the minimum average distance between point i and points in the nearest neighboring cluster. The silhouette coefficient ranges from −1 to 1, with larger values indicating stronger cluster assignment and clearer separation from other clusters. The S varied from 40 to 8, and for each condition, the average silhouette coefficient was calculated after DBSCAN-based noise removal and GMM clustering (Figure 3c). A comprehensive comparison of RG-channel intensity clustering results across all S values is provided in Figure S6. As the S decreased, s_i increased and peaked at $S = 12$. Further decrease in S reduced the number of screened flakes, limiting the statistical reliability of clustering.

The optical intensity clusters correspond to distinct MoS_2 thicknesses, as shown by AFM measurements (Figure 3d; Figure S7). The thicknesses of each cluster 1 to 6 were 2.05 ± 0.04, 2.72 ± 0.03, 3.26 ± 0.09, 3.80 ± 0.07, 4.26 ± 0.09, and 4.75 ± 0.02 nm, respectively. Considering the theoretical ML thickness of 0.65 nm for MoS_2 [32], these values correspond to 3-, 4-, 5-, 6-, 7-, and 8-ML MoS_2, respectively, with good agreement with the expected linear thickness scaling (Figure 3e). The 3-ML MoS_2 flakes correspond to the classified Level 1 in Figure 1a, while the 4- to 8-ML flakes are designated as Levels 2 through 6. Since AFM thickness measurements can slightly deviate from the theoretical values due to surface adsorbates, Raman spectroscopy was performed to further support the layer-number identification (Figure S8). The increasing Raman shift difference between the E^1_{2g} and A^1_g vibrational modes with decreasing layer number is consistent with the AFM results. The proposed optical intensity-based clustering approach enables the reliable determination of flake thickness without direct thickness measurements. This capability establishes a robust foundation for the large-scale acquisition of layer-resolved device data from single-crystal 2D materials.

MoS_2 single-flake transistors (3–8 MLs) exhibited distinct layer-dependent electrical properties. The devices were fabricated on a 4-inch wafer in a global bottom-gate configuration using a HfO_2 (20 nm) dielectric and Ni/Au (3/20 nm) electrodes (Figure 4a,b). After automated detection and coordinate verification, only flakes satisfying the geometric requirements (channel length L_{ch}: 3 μm; minimum channel width W_{ch}: 3 μm) were processed for device fabrication (Figure 4c). Importantly, flakes with a $S \leq 12$ were filtered to ensure thickness uniformity within the channel region. The W_{ch}-normalized transfer characteristics were analyzed across more than 1600 devices grouped by layer number, with the dataset comprising approximately 700 (3 MLs), 400 (4 MLs), 300 (5 MLs), 200 (6 MLs), 30 (7 MLs), and 15 (8 MLs) samples (Figure 4d). The dominance of 3–6-ML MoS_2 flakes appears to originate from the electrochemical exfoliation process, involving ion intercalation into bulk MoS_2 followed by repeated centrifugation for sediment separation. The resulting distribution is largely governed by the dispersion stability of nanoflakes in the solution environment, although the detailed mechanism has yet to be fully elucidated.

As the MoS_2 channel thickness increases from 3 to 8 MLs, the I_{ON} increased monotonically with layer number (Figure 4e), accompanied by a continuous reduction in the R_C (Figure 4f). In parallel, the V_{TH} shifted progressively toward more negative values (Figure 4g), while the SS degraded from 300 mV·dec^{-1} in 3-ML devices to values exceeding 600 mV dec^{-1} for ≥7 MLs (Figure 4h), resulting in a concomitant increase in I_{OFF} (Figure 4i). In contrast, the field-effect mobility μ_{FE} exhibited only a weak dependence on thickness across the 3–7 MLs, remaining largely invariant before slightly decreasing at the highest layer numbers (Figure 4j). Despite the clear thickness-dependent trends, device-to-device variability remained within each thickness group. This variation likely originates from differences in the flake-electrode contact region, since the channels were defined by the as-exfoliated flakes without patterning. The relationship between electrical and optical deviations was further evaluated, revealing larger performance variability in flakes located further from the RG cluster centroid (Note S2 and Figure S9).

The thickness dependence may arise from charge carrier injection efficiency and electrostatic gate-channel controllability. Multilayer MoS_2 exhibits a reduced bandgap compared with the ML, which lowers the effective Schottky barrier height and shortens the transfer length at the metal–semiconductor interface, thereby alleviating contact resistance and enhancing current injection [33, 34]. Such thickness-enabled carrier injection improvement has been reported in scaled MoS_2 and tungsten disulfide transistors, where few-layer channels exhibit enhanced immunity to contact-length scaling without substantial changes in intrinsic transport [35–37]. In contrast, increasing channel thickness weakens electrostatic gate control. The negative shift in V_{TH}, the degradation of SS, and the increase in I_{OFF} collectively indicate incomplete channel depletion in thicker multilayer channels. These trends are consistent with prior thickness-dependent studies of 2D FETs, which have shown that single-gate geometries become progressively less effective as channel thickness increases [5, 38, 39]. To minimize extrinsic influences such as defect-induced charge trapping and more clearly validate the thickness-dependent electrical characteristics, high-capacitance

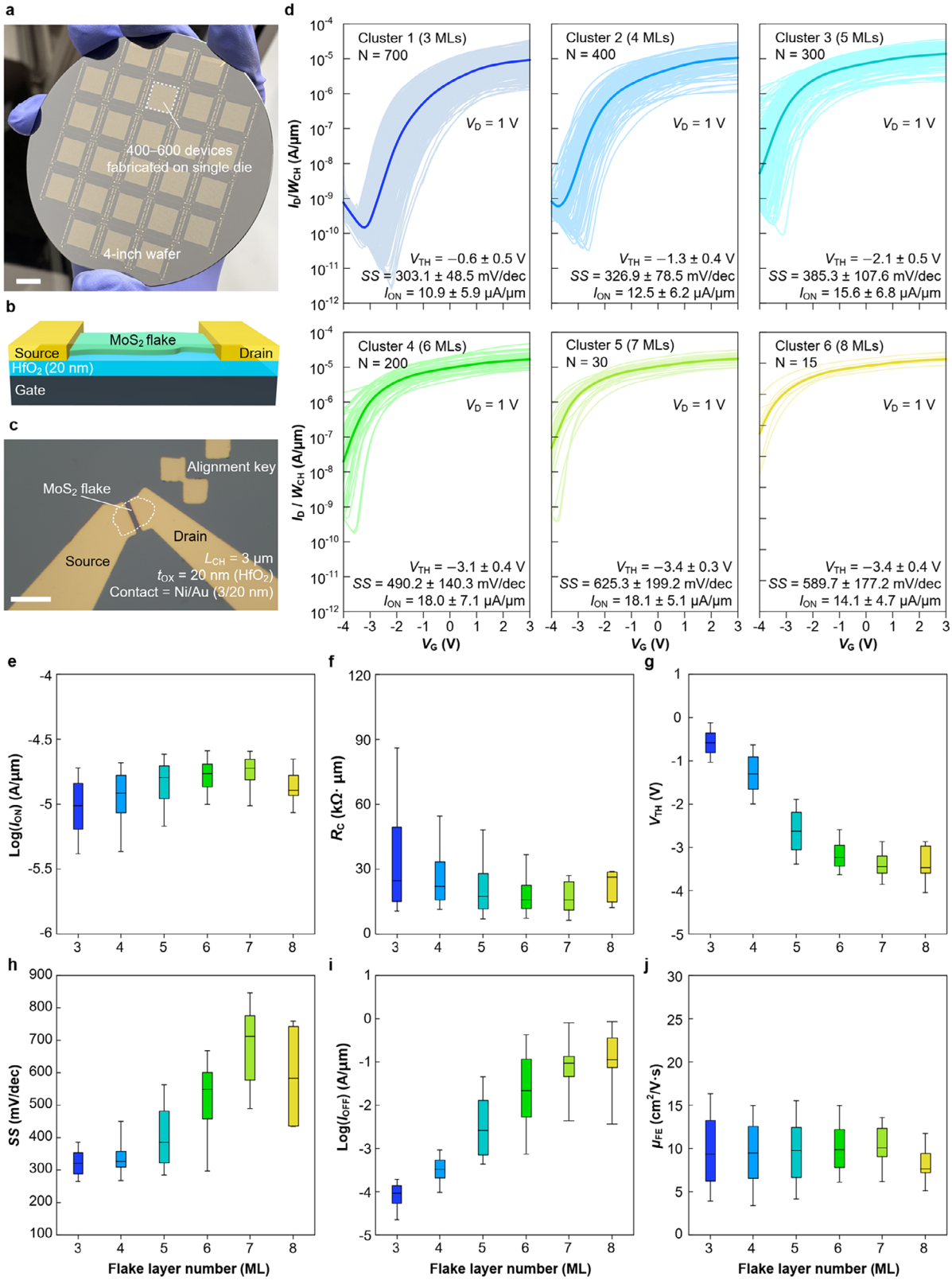

FIGURE 4 | Electrical characterization of a single flake MoS_2 transistor for different layer numbers. (a) Photograph of a 4-inch wafer (scale bar is 1 cm). (b) Optical image of the device with an automated routed electrode. (c) Schematic image of a bottom-gate single-flake MoS_2 transistor (scale bar is 20 μm). (d) Transfer characteristics of layer-by-layer single-flake MoS_2 FETs. N is the number of measured transistors. (e–j) Thickness-dependent electrical parameters of MoS_2 FETs. In each box plot, the horizontal line within the box represents the median, the box limits denote the 25th and 75th percentiles, and the whiskers indicate the minimum and maximum values. (e) $\log(I_{ON})$, (f) R_C, (g) V_{TH}, (h) SS, (i) $\log(I_{OFF})$, (j) μ_{FE} extracted where V_{DS} is +1 V.

ion-gating measurements were performed (Note S3 and Figure S10). Even under these extraordinary gate capacitance conditions (EOT < 1 nm)—where trap states are effectively filled, and non-ideal effects are neutralized—thicker flakes continued to exhibit an increased I_{OFF} and a degraded *SS*. These results indicate that thickness dependence originates from intrinsic electrostatic limitations in the multilayer channel rather than from extrinsic artifacts. For thicker channels, achieving both efficient charge injection and strong gate controllability may require 3D device geometries, such as dual-gate structures [40–43].

The large statistical dataset obtained in this study provides insight into the fundamental trade-offs governing charge transport in multilayer MoS_2 transistors. In particular, the results reveal a systematic transition from electrostatically dominated transport in thinner channels to injection-limited transport in thicker channels. While increasing the number of layers improves carrier injection by reducing contact resistance, the resulting degradation of electrostatic gate control leads to increased off-state leakage and subthreshold swing. These findings highlight the critical role of thickness engineering in balancing electrostatic control and carrier injection in 2D transistors.

Beyond the specific case of MoS_2, the automated optical-to-device workflow demonstrated here establishes a scalable experimental platform for statistically robust studies of low-dimensional semiconductor devices. By enabling the fabrication and characterization of large numbers of devices with well-defined channel thickness, this approach opens opportunities to systematically investigate variability, contact effects, and thickness-dependent transport phenomena that are difficult to capture through conventional small-sample studies.

Moreover, the statistically rich device dataset obtained in this work provides a valuable foundation for data-driven modeling of 2D transistors [44, 45]. Such datasets can support the development of compact models that incorporate thickness-dependent transport physics and device-to-device variability, enabling more realistic circuit-level simulations. Ultimately, integrating statistically grounded device models into circuit design frameworks could accelerate the development of logic and memory technologies based on atomically thin semiconductors.

3 | Conclusion

In this work, we reveal thickness-dependent charge transport in exfoliated single-flake MoS_2 transistors by linking optical thickness classification with large-scale electrical characterization. An automated optical-to-fabrication workflow classified over 120 000 flakes into thickness-defined clusters based on RG-channel intensity mapping, converting channel thickness from a stochastic outcome of exfoliation into a controlled variable. Leveraging this thickness classification, electrical characterization of 1615 MoS_2 FETs across 3 to 8 MLs establishes thickness-dependent trade-offs between electrostatic gate control and contact-limited injection. The correlation between optical thickness and electrical characteristics further suggests the potential to predict device behavior from optical signals. These results provide a thickness-resolved, data-driven pathway for understanding, and designing 2D electronic devices.

4 | Experimental Section/Methods

4.1 | Exfoliation and Characterization of MoS_2

Single-crystal MoS_2 nanosheets were prepared via an electrochemical exfoliation process [46]. Bulk MoS_2 was connected to the negative electrode, and tetrahexylammonium bromide dissolved in an acetonitrile solvent was used as the intercalating ion species. An insertion voltage in the range of 14–16 V was applied for 2 h, during which the cations were intercalated into the van der Waals gaps between MoS_2 layers. The ion-intercalated MoS_2 was subsequently sonicated for 5 min and dispersed in a DMF solution containing dissolved polyvinylpyrrolidone (PVP). The dispersion solvent consisted of 0.8892 g of PVP dissolved in 30 mL of DMF, corresponding to a concentration of 20 $mg{\cdot}mL^{-1}$. The resulting dispersion was then subjected to a three-step centrifugation process. First, the solution was centrifuged at 424 g for 5 min at 25°C, and only the supernatant was collected to remove large flakes. The collected supernatant was then centrifuged again at 12 838 g for 20 min at 25°C, after which the supernatant was discarded, and the precipitate was redispersed in 25 mL of DMF. This dispersion was centrifuged once more under the same conditions (12 838 g, 25°C, 20 min), the supernatant was removed, and the final MoS_2 dispersion was redispersed in 3 mL of DMF. The thickness and morphology of the MoS_2 sheets were characterized using atomic force microscopy (AFM, Park NX20). Optical microscopy images were acquired using an optical microscope (Leica Microsystems) at a magnification of 500×.

4.2 | Automatic Flake Detection and Routing Program

The automatic flake detection and routing program was implemented in MATLAB. A microscope equipped with a motorized stage was used to scan the entire substrate area. During image acquisition, adjacent images were stitched with an overlap of 10%. Flake positions were determined by defining the alignment key at the center of the substrate as the origin (0, 0) and calculating the coordinates based on the vector from this center point to the center of each detected flake. The image resolution was 291 044 DPI, corresponding to a pixel size of 0.08727 μm. Metal pads were pre-patterned on the substrate prior to flake deposition, and the flake solution was subsequently coated on top. Since the objective was to selectively utilize flakes above a certain size and quality threshold, flakes located too closely to each other could lead to overlaps in routing pads, and interconnects during device fabrication. To prevent this issue, the pad patterns were predefined such that one flake corresponded to each pair of the source–drain pads, and only flakes located within regularly usable regions were selected. Approximately 700 transistors could theoretically be fabricated on a single 1.5 × 1.5 cm substrate. With the current dispersion conditions, approximately 400 usable flakes were obtained per substrate.

4.3 | Device Fabrication and Electrical Characterization

Highly doped Si substrates were immersed in buffered oxide etchant for 1 min to remove the native oxide layer. Subsequently,

a 20 nm-thick HfO_2 dielectric layer was deposited at 280°C by atomic layer deposition (ALD, Lucida D100). The substrates were then patterned using maskless lithography (μMLA, Heidelberg Instruments) with a dose of 53 and a defocus value of 4, followed by deposition of Ni/Au (3/20 nm) using an electron-beam evaporator. After metal deposition, the substrates were sequentially cleaned in acetone, isopropyl alcohol, and deionized water for 10 min each. An O_2 plasma treatment was then applied, after which the MoS_2 flake dispersion was spin-coated onto the substrate at 3000 rpm for 1 min. Using the automatic flake detection and routing program, a lithography-ready layout containing the source–drain interconnects was generated. Based on this layout, the source–drain electrodes were patterned using the same maskless lithography conditions (dose 53, defocus 4), followed by deposition of Ni/Au (3/20 nm) via electron-beam evaporation. The samples were then immersed in DPS at 70°C overnight, followed by a 30 s power-2 sonication in acetone for lift-off. Electrical measurements were carried out at 25°C under ambient conditions using a Keysight B1500 semiconductor parameter analyzer.

Acknowledgements

This work was funded by the National Research Foundation of Korea(NRF) grant funded by the Korea government(MSIT)(RS-2024-00355384), supported by the Korea Planning & Evaluation Institute of Industrial Technology(KEIT) (RS-2024-00417909) funded by the Ministry of Trade, Industry & Energy(MOTIE, Korea), supported by Quantum Common Core Technology R&D Program(RS-2025-25457200) through the National Research Foundation of Korea(NRF) funded by the Korean government (Ministry of Science and ICT(MSIT)), and also supported by the Commercialization Promotion Agency for R&D Outcomes(COMPA) funded by the Ministry of Science and ICT(MSIT)(Grant No. 2710086066).

Conflicts of Interest

The authors declare no conflicts of interest.

Data Availability Statement

The data that support the findings of this study are available from the corresponding author upon reasonable request.

References

1. M. Chhowalla, D. Jena, and H. Zhang, "Two-Dimensional Semiconductors for Transistors," *Nature Reviews Materials* 1 (2016): 16052, https://doi.org/10.1038/natrevmats.2016.52.

2. Y. Liu, X. Duan, H. J. Shin, S. Park, Y. Huang, and X. Duan, "Promises and Prospects of Two-Dimensional Transistors," *Nature* 591 (2021): 43–53, https://doi.org/10.1038/s41586-021-03339-z.

3. H. Jung, J. Choi, S. Baek, et al., "Advances and Future Challenges in Monolithic 3D Integrated Logic, Power, and Optoelectronics Technologies for Tightly Interconnected Intelligent Systems," *ACS Nano* 20 (2026): 6407–6445, https://doi.org/10.1021/acsnano.5c15601.

4. J.-H. Kang, H. Shin, K. S. Kim, et al., "Monolithic 3D Integration of 2D Materials-Based Electronics Towards Ultimate Edge Computing Solutions," *Nature Materials* 22 (2023): 1470–1477, https://doi.org/10.1038/s41563-023-01704-z.

5. B. Radisavljevic, A. Radenovic, J. Brivio, V. Giacometti, and A. Kis, "Single-Layer MoS_2 Transistors," *Nature Nanotechnology* 6 (2011): 147–150, https://doi.org/10.1038/nnano.2010.279.

6. J. Jiang, L. Xu, C. Qiu, and L. M. Peng, "Ballistic Two-Dimensional InSe Transistors," *Nature* 616 (2023): 470–475, https://doi.org/10.1038/s41586-023-05819-w.

7. F. Wu, H. Tian, Y. Shen, et al., "Vertical MoS_2 Transistors With Sub-1-nm Gate Lengths," *Nature* 603 (2022): 259–264, https://doi.org/10.1038/s41586-021-04323-3.

8. B. Tang, M. Sivan, J. F. Leong, et al., "Solution-Processable 2D Materials for Monolithic 3D Memory-Sensing-Computing Platforms: Opportunities and Challenges," *npj 2D Materials and Applications* 8 (2024): 74, https://doi.org/10.1038/s41699-024-00508-2.

9. J. Suh, T. L. Tan, W. Zhao, et al., "Reconfiguring Crystal and Electronic Structures of MoS_2 by Substitutional Doping," *Nature Communications* 9 (2018): 199, https://doi.org/10.1038/s41467-017-02631-9.

10. Y. Yoon, K. Ganapathi, and S. Salahuddin, "How Good can Monolayer MoS_2 Transistors be?," *Nano Letters* 11 (2011): 3768–3773, https://doi.org/10.1021/nl2018178.

11. J. Zheng, H. Zhang, S. Dong, et al., "High Yield Exfoliation of Two-Dimensional Chalcogenides Using Sodium Naphthalenide," *Nature Communications* 5 (2014): 2995, https://doi.org/10.1038/ncomms3995.

12. X. Zhu, D. Li, R. Zhang, et al., "Probing Quantum Confinement Effects on the Excitonic Property and Electronic Band Structures of MoS_2," *Applied Surface Science* 519 (2020): 146262, https://doi.org/10.1016/j.apsusc.2020.146262.

13. P. Borah, D. Siboh, P. K. Kalita, J. K. Sarma, and N. M. Nath, "Quantum Confinement Induced Shift in Energy Band Edges and Band Gap of a Spherical Quantum Dot," *Physica B: Condensed Matter* 530 (2018): 208–214, https://doi.org/10.1016/j.physb.2017.11.046.

14. T. Edvinsson, "Optical Quantum Confinement and Photocatalytic Properties in Two-, One- and Zero-Dimensional Nanostructures," *Royal Society Open Science* 5 (2018): 180387, https://doi.org/10.1098/rsos.180387.

15. J. Kang, L. Zhang, and S.-H. Wei, "A Unified Understanding of the Thickness-Dependent Bandgap Transition in Hexagonal Two-Dimensional Semiconductors," *The Journal of Physical Chemistry Letters* 7 (2016): 597–602, https://doi.org/10.1021/acs.jpclett.5b02687.

16. Z. G. Yu, B. I. Yakobson, and Y.-W. Zhang, "Realizing Indirect-to-Direct Band Gap Transition in Few-Layer Two-Dimensional MX_2 (M = Mo, W; X = S, Se)," *ACS Applied Energy Materials* 1 (2018): 4115–4121, https://doi.org/10.1021/acsaem.8b00774.

17. R. Dhall, M. R. Neupane, D. Wickramaratne, et al., "Direct Bandgap Transition in Many-Layer MoS_2 by Plasma-Induced Layer Decoupling," *Advanced Materials* 27 (2015): 1573–1578, https://doi.org/10.1002/adma.201405259.

18. X. Li, W. Han, J. Wu, X. Qiao, J. Zhang, and P. Tan, "Layer-Number Dependent Optical Properties of 2D Materials and Their Application for Thickness Determination," *Advanced Functional Materials* 27 (2017): 1604468, https://doi.org/10.1002/adfm.201604468.

19. C. Yim, M. O'Brien, N. McEvoy, et al., "Investigation of the Optical Properties of MoS_2 Thin Films Using Spectroscopic Ellipsometry," *Applied Physics Letters* 104 (2014): 103114, https://doi.org/10.1063/1.4868108.

20. D. Li, X. Song, J. Xu, et al., "Optical Properties of Thickness-Controlled MoS_2 Thin Films Studied by Spectroscopic Ellipsometry," *Applied Surface Science* 421 (2017): 884–890, https://doi.org/10.1016/j.apsusc.2016.09.069.

21. S. Wang, J. Xue, D. Xu, et al., "Electrochemical Molecular Intercalation and Exfoliation of Solution-Processable Two-Dimensional Crystals," *Nature Protocols* 18 (2023): 2814–2837, https://doi.org/10.1038/s41596-023-00865-0.

22. Y. Huang, Y.-H. Pan, R. Yang, et al., "Universal Mechanical Exfoliation of Large-Area 2D Crystals," *Nature Communications* 11 (2020): 2453, https://doi.org/10.1038/s41467-020-16266-w.

23. Q. Wang, N. Li, J. Tang, et al., "Wafer-Scale Highly Oriented Monolayer MoS_2 With Large Domain Sizes," *Nano Letters* 20 (2020): 7193–7199, https://doi.org/10.1021/acs.nanolett.0c02531.

24. Y. Xia, X. Chen, J. Wei, et al., "12-Inch Growth of Uniform MoS_2 Monolayer for Integrated Circuit Manufacture," *Nature Materials* 22 (2023): 1324–1331, https://doi.org/10.1038/s41563-023-01671-5.

25. J.-L. Uslu, T. Ouaj, D. Tebbe, et al., "An Open-Source Robust Machine Learning Platform for Real-Time Detection and Classification of 2D Material Flakes," *Machine Learning: Science and Technology* 5 (2024): 015027, https://doi.org/10.1088/2632-2153/ad2287.

26. B. S. Jessen, P. R. Whelan, D. M. A. Mackenzie, et al., "Quantitative Optical Mapping of Two-Dimensional Materials," *Scientific Reports* 8 (2018): 6381, https://doi.org/10.1038/s41598-018-23922-1.

27. Y. Saito, K. Shin, K. Terayama, et al., "Deep-Learning-Based Quality Filtering of Mechanically Exfoliated 2D Crystals," *npj Computational Materials* 5 (2019): 124, https://doi.org/10.1038/s41524-019-0262-4.

28. S. Yan, J. Chen, X. Li, et al., "Large Scale and Diverse Two-Dimensional Flake Segmentation Dataset by General-Purpose and Labor-Efficient Annotation Framework," *npj 2D Materials and Applications* 9 (2025): 103, https://doi.org/10.1038/s41699-025-00622-9.

29. P. A. Leger, A. Ramesh, T. Ulloa, and Y. Wu, "Machine Learning Enabled Fast Optical Identification and Characterization of 2D Materials," *Scientific Reports* 14 (2024): 27808, https://doi.org/10.1038/s41598-024-79386-z.

30. J.-L. Uslu, A. Nekrasov, A. Hermans, et al., "MaskTerial: A Foundation Model for Automated 2D Material Flake Detection," arXiv **(2024)**: arXiv 2412.09333, https://arxiv.org/abs/2412.09333.

31. H. Jung, M. Kim, Y. Lee, et al., "Back-End-of-Line-Compatible Passivation of Sulfur Vacancies in MoS_2 Transistors Using Electron-Withdrawing Benzenethiol," *ACS Nano* 19 (2025): 6069–6078, https://doi.org/10.1021/acsnano.4c12927.

32. S. Zhou, W. Ma, U. Anjum, et al., "Strained Few-Layer MoS_2 With Atomic Copper and Selectively Exposed In-Plane Sulfur Vacancies for CO_2 Hydrogenation to Methanol," *Nature Communications* 14 (2023): 5872, https://doi.org/10.1038/s41467-023-41362-y.

33. K. F. Mak, C. Lee, J. Hone, J. Shan, and T. F. Heinz, "Atomically Thin MoS_2: A New Direct-Gap Semiconductor," *Physical Review Letters* 105 (2010): 136805, https://doi.org/10.1103/PhysRevLett.105.136805.

34. K. Kim, S. Coh, L. Z. Tan, et al., "Raman Spectroscopy Study of Rotated Double-Layer Graphene: Misorientation-Angle Dependence of Electronic Structure," *Physical Review Letters* 108 (2012): 246103, https://doi.org/10.1103/PhysRevLett.108.246103.

35. D. S. Schulman, A. J. Arnold, and S. Das, "Contact Engineering for 2D Materials and Devices," *Chemical Society Reviews* 47 (2018): 3037–3058, https://doi.org/10.1039/C7CS00828G.

36. N. U. Sakib, C. Chen, L. Ding, Y. Yang, J. M. Redwing, and S. Das, "High-Performance Molybdenum Disulfide Transistors With Channel and Contact Lengths Below 35 nm," *Nature Electronics* 8 (2025): 1201–1210, https://doi.org/10.1038/s41928-025-01499-8.

37. R. Kappera, D. Voiry, S. E. Yalcin, et al., "Phase-Engineered Low-Resistance Contacts for Ultrathin MoS_2 Transistors," *Nature Materials* 13 (2014): 1128–1134, https://doi.org/10.1038/nmat4080.

38. Y. Zhang, H. Li, H. Wang, et al., "Direct Observation of the Transition From Indirect to Direct Bandgap in Atomically Thin Epitaxial $MoSe_2$," *Nature Natnotechnology* 9 (2014): 111–115, https://doi.org/10.1038/nnano.2013.277.

39. D. Sharma, A. Motayed, P. B. Shah, et al., "Transfer Characteristics and Low-Frequency Noise in Single- and Multi-Layer MoS_2 Field-Effect Transistors," *Applied Physics Letters* 107 (2015): 162102, https://doi.org/10.1063/1.4932945.

40. J. Kwon, Y. Takeda, R. Shiwaku, S. Tokito, K. Cho, and S. Jung, "Three-Dimensional Monolithic Integration in Flexible Printed Organic Transistors," *Nature Communications* 10 (2019): 54, https://doi.org/10.1038/s41467-018-07904-5.

41. X. Wu, D. Cott, Z. Lin, et al., "Dual Gate Synthetic MoS2 MOSFETs with 4.56μF/cm^2 Channel Capacitance, 320μS/μm Gm and 420 μA/μm Id at 1V Vd/100nm Lg," paper presented at 2021 IEEE International Electron Devices Meeting (IEDM), (IEEE, 2021), 7.4.1–7.4.4, https://doi.org/10.1109/IEDM19574.2021.9720695.

42. G. Bae, D.-I. Bae, M. Kang, et al., "3nm GAA Technology Featuring Multi-Bridge-Channel FET for Low Power and High Performance Applications," paper presented at 2018 IEEE International Electron Devices Meeting (IEDM), (IEEE, 2018), 28.7.1–28.7.4, https://doi.org/10.1109/IEDM.2018.8614629.

43. Y. Lee, H. Jung, Y. Jo, et al., "Dual-Gate Carbon Nanotube Thin-Film Transistors With Printed Channel and Passivation Interlayer on Plastic Foil," *IEEE Electron Device Letters* 45 (2024): 2036–2039, https://doi.org/10.1109/LED.2024.3440484.

44. C. Park, S. Lee, J. Park, et al., "Large-Scale Training in Neural Compact Models for Accurate and Adaptable MOSFET Simulation," *IEEE Journal of the Electron Devices Society* 12 (2024): 745–751, https://doi.org/10.1109/JEDS.2024.3417521.

45. Y. S. Cha, J. Park, C. Park, et al., "A Novel Methodology for Neural Compact Modeling Based on Knowledge Transfer," *Solid-State Electronics* 198 (2022): 108450, https://doi.org/10.1016/j.sse.2022.108450.

46. Z. Lin, Y. Liu, U. Halim, et al., "Solution-Processable 2D Semiconductors for High-Performance Large-Area Electronics," *Nature* 562 (2018): 254–258, https://doi.org/10.1038/s41586-018-0574-4.

Supporting Information

Additional supporting information can be found online in the Supporting Information section.

Supporting File: adfm74979-sup-0001-SuppMat.docx.